

# On effects of surface bipolar magnetic regions on the convection zone dynamo

V.V. Pipin,<sup>\*</sup>

*Institute of Solar-Terrestrial Physics, Russian Academy of Sciences, Irkutsk, 664033, Russia*

23 May 2022

## ABSTRACT

We investigate the effect of the surface bipolar magnetic regions (BMR) on the large-scale dynamo distributed in the bulk of the convection zone. The study employs the nonlinear 3D mean-field dynamo model. We model the emergence of the BMR on the surface through the nonaxisymmetric magnetic buoyancy effect, which acts on the large-scale toroidal magnetic field in the upper half of the convection zone. The nonaxisymmetric magnetic field which results from this mechanism is shallow. On the surface, the effect of the BMR on the magnetic field generation is dominant. However, because of the shallow BMR distribution, its effect on the global dynamo is less compared to the convective zone dynamo. We find that the mean-field  $\alpha$  effect, which acts on the nonaxisymmetric magnetic field of the BMRs, provides the greater contribution to the dynamo process than the BMR's tilt does. Even so, the fluctuations of the BMR's tilt lead to the parity braking in the global dynamo. At the surface the nonaxisymmetric magnetic field, which are generated because of the BMR's activity, shows a tendency for the bihelical spectrum with the positive sign for the low  $\ell$  modes during the maximum of the magnetic activity cycle.

**Key words:** Sun: magnetic fields; Sun: oscillations; sunspots

## 1 INTRODUCTION

Parker (1955) represented the whole dynamo process as the dynamo waves propagating through the convection zone. This idea grew to the mean-field MHD and dynamo theory (Moffatt (1978); Krause & Rädler (1980)). The mean-field theory framework employs the idea of the scale separation between the mean and turbulent parts of the magnetic field and flow. It assumes that the mean large-scale field can be extracted from the background turbulent astrophysical plasma using an appropriate averaging procedure (see the above-cited textbooks). In the solar-type dynamos, the axisymmetric magnetic field dominates. On the Sun, the large-scale nonaxisymmetric dynamo is well below the dynamo instability threshold because of differential rotation (Raedler (1986)). Yet, most of the energy of the surface magnetic field is concentrated on small scales (Vidotto et al. 2018). The origin of the surface nonaxisymmetric magnetic fields seems to be connected with the emergence and decay of solar active regions (Wang et al. 1989).

The effect of the surface magnetic activity on the large-scale dynamo is poorly understood. One way to account for it is through the boundary conditions. Under the insulator boundary condition, the external magnetic field is potential, and the toroidal magnetic field is zero at the surface. Observations show that more realistic boundary conditions should allow penetration of the toroidal magnetic field to the sur-

face (Moss & Brandenburg (1992); Bonanno (2016)). Note that the penetration of the toroidal magnetic field to the surface allows the efficient poloidal magnetic field generation in the near-surface layer.

The Babcock-Leighton scenario accounts for the surface magnetic activity on the dynamo phenomenologically (Babcock 1961 and Leighton 1964). The phenomenological picture behind it was established and summarized in several papers and reviews (see, e.g., Giovanelli 1985; Wang et al. 1989; Petrie et al. 2014). This scenario is employed in the flux transport dynamo models (see Mackay & Yeates 2012; Ugarte-Urra et al. 2015; Cameron & Schüssler 2017 and references therein). In this scenario, the tilted BMRs emerging and developing at the surface result in the dynamo generation of the poloidal magnetic field of the Sun. In the convection zone dynamo scenario, the regeneration of the poloidal magnetic field goes everywhere in the depth of the convection zone.

Results of the flux transport dynamo models (see, Karak et al. 2014; Passos et al. 2014; Hazra & Nandy 2019) show the necessity of the mean-field effects to account for the possible complicated properties of the global flow and properties of the long-term variations of the solar activity. Yet, the simple framework of the Babcock-Leighton scenario faces problems to reproduce the results of the global convection dynamo simulation (see, Schrunner (2011); Schrunner et al. (2011); Warnecke et al. (2021)). This is because of a poor representation of the mean electromotive force of turbulent flows and magnetic fields. In this paper, we consider the mean-field dy-

\* email: pip@iszf.irk.ru

namo model of [Pipin & Kosovichev \(2019\)](#). To account for the dynamo effects of bipolar magnetic regions, the model prescribes the nonaxisymmetric magnetic buoyancy and  $\alpha$  effects acting on the buoyant part of the toroidal magnetic field.

## 2 MODEL

In this study, we employ the mean-field MHD framework, which was formulated by [Roberts & Soward \(1975\)](#) and [Krause & Rädler \(1980\)](#) to describe the evolution of the large-scale magnetic field in the turbulent astrophysical plasma. The model solves the dynamo equations together with the equations governing the angular momentum balance, meridional circulation and the mean heat transport in the convection zone.

### 2.1 Mean-field dynamo equations

The magnetic field evolution is governed by the mean-field induction equation:

$$\partial_t \langle \mathbf{B} \rangle = \nabla \times (\mathcal{E} + \langle \mathbf{U} \rangle \times \langle \mathbf{B} \rangle), \quad (1)$$

where  $\mathcal{E} = \langle \mathbf{u} \times \mathbf{b} \rangle$  is the mean electromotive force;  $\mathbf{u}$  and  $\mathbf{b}$  are the turbulent fluctuating velocity and magnetic field, respectively; and  $\langle \mathbf{U} \rangle$  and  $\langle \mathbf{B} \rangle$  are the mean velocity and magnetic field. We assume that the averaging is done over the ensemble of turbulent flows and magnetic fields. Like [Moss et al. \(1991\)](#), we represent the vector  $\langle \mathbf{B} \rangle$  by sum of the axisymmetric and nonaxisymmetric parts. These parts are further decomposed into a sum of the poloidal and toroidal components, as follows:

$$\langle \mathbf{B} \rangle = \bar{\mathbf{B}} + \tilde{\mathbf{B}}, \quad (2)$$

$$\bar{\mathbf{B}} = \hat{\phi} B + \nabla \times (A \hat{\phi}), \quad (3)$$

$$\tilde{\mathbf{B}} = \nabla \times (\mathbf{r}T) + \nabla \times \nabla \times (\mathbf{r}S), \quad (4)$$

where  $\bar{\mathbf{B}}$  and  $\tilde{\mathbf{B}}$  are the axisymmetric and nonaxisymmetric components of the large-scale magnetic field. Also,  $\hat{\phi}$  is the azimuthal unit vector,  $\mathbf{r}$  is the radius vector,  $r$  is the radial distance, and  $\theta$  is the polar angle. The gauge transformation for superpotentials  $T$  and  $S$  involves a sum with the arbitrary  $r$ -dependent function ([Krause & Rädler 1980](#)). We seek the solution for  $T$  and  $S$  using the spherical harmonic decomposition. In this case, by definition, the zero  $\ell$  modes are excluded. In this case, the representation of the Eq(4) is gauge invariant (also, see, [Berger & Hornig 2018](#)). We assume that the large-scale flow is axisymmetric  $\langle \mathbf{U} \rangle \equiv \bar{\mathbf{U}}$ . Similarly, we assume that the mean entropy and the other thermodynamic parameters are axisymmetric, as well. Nevertheless, the model takes into account the effect of the nonaxisymmetric magnetic field on the angular momentum balance and the meridional circulation using the longitudinal averaging of the Lorentz force. To get the dynamo equations for the axisymmetric toroidal magnetic field evolution, we take the scalar product of the Eq(1) with the unit vector  $\hat{\phi}$ . We do the same for the uncurled version the Eq(1) to get the equation for the vector potential  $A$ . To get the evolution equations for the nonaxisymmetric magnetic field we take the curl and double curl of the Eq(1). Then, we take the scalar product of these

equations with vector  $\mathbf{r}$  (see, details in [Krause & Rädler 1980](#), and [Moss et al. 1991](#)).

We decompose the mean electromotive force for two parts:

$$\mathcal{E}_i = \mathcal{E}_i^{(A)} + \mathcal{E}_i^{(\text{BMR})}, \quad (5)$$

where the expression for  $\mathcal{E}_i^{(A)}$  results from the analytical computations (see, e.g., [Kitchatinov et al. 1994](#); [Pipin 2008](#)). The  $\mathcal{E}_i^{(\text{BMR})}$  stands for the phenomenological part of mean electromotive force. I introduce it to take the effects of the BMRs into account.

The  $\mathcal{E}_i^{(A)}$  reads as follows,

$$\mathcal{E}_i^{(A)} = (\alpha_{ij} + \gamma_{ij}) \langle B \rangle_j - \eta_{ijk} \nabla_j \langle B \rangle_k, \quad (6)$$

where the tensor,  $\alpha_{ij}$  stands for the turbulent generation by  $\alpha$ -effect,  $\gamma_{ij}$  is the turbulent pumping and  $\eta_{ijk}$  is the eddy magnetic diffusivity tensor. The analytical expressions of the  $\alpha_{ij}$ ,  $\gamma_{ij}$  and  $\eta_{ijk}$  take into account effects of the global rotation, magnetic field and density stratification on the turbulent convection. The same model was recently considered by [Pipin & Kosovichev \(2019\)](#) and [Pipin & Kosovichev \(2020\)](#). For convenience, we present the full expressions of the above tensors in Appendix A.

The  $\alpha$  effect tensor includes the small-scale magnetic helicity density contribution, i.e., the pseudo scalar  $\langle \chi \rangle = \langle \mathbf{a} \cdot \mathbf{b} \rangle$  (where  $\mathbf{a}$  and  $\mathbf{b}$  are the fluctuating vector-potential and magnetic field, respectively),

$$\alpha_{ij} = C_\alpha \psi_\alpha(\beta) \alpha_{ij}^{(H)} + \alpha_{ij}^{(M)} \psi_\alpha(\beta) \frac{\langle \chi \rangle \tau_c}{4\pi \bar{\rho} \ell_c^2}, \quad (7)$$

where, the contributions of the kinetic  $\alpha$  effect tensor  $\alpha_{ij}^{(H)}$  and the magnetic helicity effect tensor  $\alpha_{ij}^{(M)}$  are given in Appendix A. The radial profiles of the  $\alpha_{ij}^{(H)}$  and  $\alpha_{ij}^{(M)}$  depend on the mean density stratification, the profile of the convective RMS velocity  $u_c$  and on the Coriolis number  $\Omega^* = 2\Omega_0 \tau_c$ , where  $\Omega_0$  is the angular velocity of the star and  $\tau_c$  is the convective turnover time. The magnetic quenching function  $\psi_\alpha(\beta)$  depends on the parameter  $\beta = |\langle \mathbf{B} \rangle| / \sqrt{4\pi \bar{\rho} u_c^2}$  (see Appendix A). Note that in the presence of the  $\mathbf{B}$ -field, the  $\alpha$  effect tensor becomes nonaxisymmetric. This effect is caused both by the  $\psi_\alpha(\beta)$ -quenching and the magnetic helicity effects.

The magnetic helicity evolution follows the global conservation law for the total magnetic helicity,  $\langle \chi \rangle^{(tot)} = \langle \chi \rangle + \langle \mathbf{A} \rangle \cdot \langle \mathbf{B} \rangle$ , (see, [Hubbard & Brandenburg \(2012\)](#); [Pipin et al. \(2013\)](#); [Brandenburg \(2018\)](#)):

$$\left( \frac{\partial}{\partial t} + \langle \mathbf{U} \rangle \cdot \nabla \right) \langle \chi \rangle^{(tot)} = - \frac{\langle \chi \rangle}{R_m \tau_c} - 2\eta \langle \mathbf{B} \rangle \cdot \langle \mathbf{J} \rangle - \nabla \cdot \mathcal{F}^\chi, \quad (8)$$

where, we use  $2\eta \langle \mathbf{b} \cdot \mathbf{j} \rangle = \frac{\langle \chi \rangle}{R_m \tau_c}$  ([Kleeorin & Rogachevskii 1999](#)). Also, we introduce the diffusive flux of the small-scale magnetic helicity density,  $\mathcal{F}^\chi = -\eta_\chi \nabla \langle \chi \rangle$ , and  $R_m$  is the magnetic Reynolds number. The coefficient of the turbulent helicity diffusivity,  $\eta_\chi$ , is chosen ten times smaller than the isotropic part of the magnetic diffusivity [Mitra et al. \(2010\)](#):  $\eta_\chi = \frac{1}{10} \eta_T$ .

The mean magnetic helicity density is formally decomposed into the axisymmetric and nonaxisymmetric parts:  $\langle \chi \rangle^{(tot)} = \bar{\chi}^{(tot)} + \tilde{\chi}^{(tot)}$ . The same is done for the magnetic helicity density of the turbulent field:  $\langle \chi \rangle = \bar{\chi} + \tilde{\chi}$ , here  $\bar{\chi} = \overline{\mathbf{a} \cdot \mathbf{b}}$  and

$\tilde{\chi} = \langle \mathbf{a} \cdot \tilde{\mathbf{b}} \rangle$ . Thus, we have,

$$\bar{\chi}^{(tot)} = \bar{\chi} + \bar{\mathbf{A}} \cdot \bar{\mathbf{B}} + \overline{\tilde{\mathbf{A}} \cdot \tilde{\mathbf{B}}}, \quad (9)$$

$$\tilde{\chi}^{(tot)} = \tilde{\chi} + \bar{\mathbf{A}} \cdot \tilde{\mathbf{B}} + \tilde{\mathbf{A}} \cdot \bar{\mathbf{B}} + \tilde{\mathbf{A}} \cdot \tilde{\mathbf{B}}, \quad (10)$$

The evolution of the  $\bar{\chi}$  and  $\tilde{\chi}$  is governed by the corresponding parts of Eq(8). The magnetic helicity conservation is determined by the magnetic Reynolds number  $R_m$ . In this paper, we employ  $R_m = 10^6$ .

## 2.2 The BMR's formation and its dynamo effects

To take into account the effects of the surface bipolar magnetic regions (BMRs) on the dynamo, we introduce the phenomenological part of the mean electromotive force as follows,

$$\mathcal{E}_i^{(\text{BMR})} = \alpha_\beta \delta_{i\phi} \langle B \rangle_\phi + V_\beta (\hat{\mathbf{r}} \times \langle \mathbf{B} \rangle)_i, \quad (11)$$

where the first term takes into account the BMR's  $\alpha$ -effect and the second term does the same for the magnetic buoyancy effect. Our motivation for the Eq.(11) following Parker (1979) idea. We assume that some part of the toroidal magnetic field in the upper part of the convection zone becomes buoyantly unstable, it emerges and forms the surface BMR. The second term of the Eq.(11) describes the buoyant emergence of the BMR. Later we will see, that the first term of this formula is related with the BMR's tilt. A mechanism of the instability can be rather complicated (see, e.g., Gilman 1970, 2018). Also, it is likely, that other processes in the solar convection zone can be responsible for the BMRs formations (see, e.g., Kleorin et al. 1989; Kitchatinov & Mazur 2000; Getling 2001; Brandenburg et al. 2013; Stein & Nordlund 2012; Losada et al. 2017; Kleorin et al. 2020). Here, the model employs the magnetic buoyancy effect formally. Its main goal is to mimic the BMRs on the solar surface. Other implementations of the BMRs can be found in the models of the Babcock-Leighton type (see, e.g., Yeates et al. 2008; Brun et al. 2014; Miesch & Dikpati 2014).

The magnetic buoyancy velocity is modeled using the turbulent and mean-field buoyancy effects. Its expression was suggested earlier (see, Kitchatinov & Rüdiger 1992; Kitchatinov & Pipin 1993; Ruediger & Brandenburg 1995). Following these results we put,

$$V_\beta = V_m \xi_\beta(t, \mathbf{r}) \quad (12)$$

$$V_m = \frac{\alpha_M u_c}{\gamma} \mathcal{H}(\beta_m), \quad (13)$$

where  $\alpha_M = 1.9$  is the mixing-length theory parameter,  $\gamma$  is the adiabatic law constant,  $u_c$  is the convective RMS velocity and  $\beta = |\langle \mathbf{B} \rangle| / \sqrt{4\pi\bar{\rho}u_c^2}$ . The function  $\mathcal{H}(\beta)$  takes into account the effect of the magnetic tensions on the mean-field magnetic buoyancy (see, Appendix A). The subscript 'm' in the Eq(12) marks that the amplitude of the effect is taken at the location of maximum of the magnetic field strength. Note, that the turbulent pumping tensor,  $\gamma_{ij}$ , in the Eq.(6) take into account the mean-field magnetic buoyancy, as well, (though there we have  $\xi_\beta = 0$  and smooth profile of  $\mathcal{H}(\beta)$  corresponding to the B-field distribution). The spatial and temporal parameters of the  $\xi_\beta$  are controlled by the formula,

$$\xi_\beta(\mathbf{r}, t) = \psi(r, t) \exp\left(-m_\beta \left(\sin^2\left(\frac{\phi - \phi_m}{2}\right) + \sin^2\left(\frac{\theta - \theta_m}{2}\right)\right)\right), \quad (14)$$

where  $\psi$  is a kink type function of radius and time,

$$\begin{aligned} \psi &= \frac{1}{2} (1 - \text{erf}(50(r - r_m))) e^{t/\tau_0}, t < \delta t \\ &= 0, t > \delta t., \end{aligned} \quad (15)$$

where  $r_m$  and  $\theta_m$  are the radius and the latitude of the toroidal magnetic field strength extrema in the upper part of the convection zone. The other parameters in the Eqs(14,15) are as follows. We put the emergence time,  $\delta t$  to 5 days. The parameter  $\tau_0$  controls the growth rate of the BMRs. In our simulations, we put  $\tau_0 = 1$  day, which roughly corresponds to the results of Stenflo & Kosovichev (2012)). The longitudinal coordinate  $\phi_m$  is random. The similar parameters of  $\delta t$  and  $\tau_0$  are employed in the spotmaker module of the 3D Babcock-Leighton model of Miesch & Dikpati (2014). The size of the BMR is controlled by the parameter,  $m_\beta$ . In the paper, we put  $m_\beta = 100$ . This results in about  $10^\circ$  separation between the leading and following polarity of the BMR. The nonaxisymmetric perturbations,  $\xi_\beta$ , are randomly initiated in time and longitude in each hemisphere independently. The parameters  $\delta t$ ,  $\tau_0$ , and  $m_\beta$  affect the magnetic flux of the BMR and the total magnetic flux generated by the BMRs. In our model, the magnitude of the magnetic flux of the typical BMR is around  $4\text{-}5 \cdot 10^{22}$  Mx. The decrease of  $\tau_0$ , and  $m_\beta$  and the increase of  $\delta t$  results in the increase of the magnetic flux of the emerging BMR.

In following of Parker (1979), it is assumed that the large-scale toroidal magnetic field becomes unstable, when its strength decreases outward faster than the mean density does. In particular, we compute the parameter

$$I_\beta = -r \frac{\partial}{\partial r} \log \frac{|\bar{B}|^\zeta}{\bar{\rho}}, \quad (16)$$

where  $\bar{B}$  is the strength of the axisymmetric toroidal magnetic field and  $\bar{\rho}$  is the density profile. For the case of  $\zeta = 1$  we get the Parker's instability condition. In this case, we find that the BMR's productivity is not enough to reproduce the solar observations. In our simulations we use  $\zeta = 1.2$ . The dependence of  $\zeta$  parameter on the physical conditions in the stellar convection zone deserves a separate study and it is out of our scope for this paper. The  $\xi_\beta(\mathbf{r}, t)$  is initiated when and if  $I_\beta(r_m, \theta_m) > 0$ . In addition, we restrict the instability region using the following conditions:  $r_m > 0.85R$  and  $|\bar{B}_m| > 500\text{G}$ .

The  $\alpha$ -effect of the  $\mathcal{E}^{(\text{BMR})}$  is given as follows

$$\alpha_\beta = C_{\alpha\beta} (1 + \xi_\alpha) \cos \theta V_\beta \psi_\alpha(\beta). \quad (17)$$

Here, we put the amplitude of the  $\alpha$ -effect to be determined by the local magnetic buoyancy velocity. The  $\xi_\alpha$  parameter controls the random fluctuation of the BMR's  $\alpha$ -effect. The parameter,  $C_{\alpha\beta}$  controls the amplitude of the BMR's  $\alpha$ -effect and tilt in the different simulation runs (see the Subsection 2.4). The Fig1 shows that the nonlinear profiles of the  $\mathcal{H}(\beta)$  and  $\psi(\beta)$  put the limits on the magnitude of the possible buoyancy velocity drift and the corresponded  $\alpha_\beta$  effect. The velocity drift is order of  $V_m \sim \frac{1}{40} u_c$  for the  $\beta \sim 1$  and the  $\alpha_\beta$  is the order of magnitude smaller. The mean-field solar dynamo models of Pipin & Kosovichev (2020) operates in the weakly nonlinear regime where  $\beta \leq 0.2$ . In this case,  $V_m \sim 10^{-3} u_c$ .

The Fig.2 shows the relation between the magnitude of the BMR's  $\alpha$ -effect and tilt for the latitude  $25^\circ$ . To calculate this

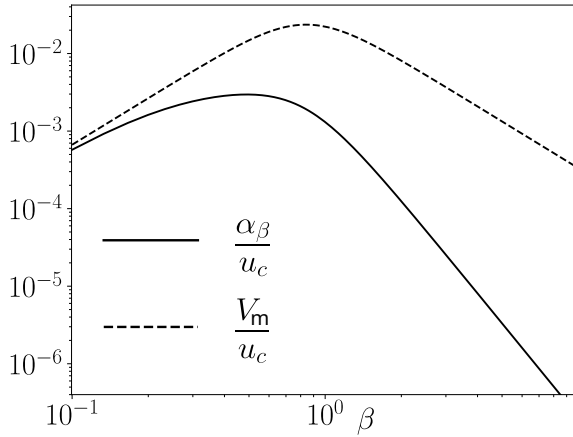


**Figure 1.** Connection of the mean-field buoyancy velocity (dashed line) and the  $\alpha_\beta$  effect (solid line) with the magnetic field strength parameter  $\beta$ .

relation, we used the short runs. Each run starts with the pure axisymmetric magnetic field distribution, which is shown in the Fig3a. The BMR is injected in the northern hemisphere of the Sun. We assume that the axis of the BMR connects the extrema points of opposite polarities. The positive tilt corresponds to Joy’s law. For the case  $C_{\alpha\beta} = 0.5$ , the tilt of the BMRs is about  $10^\circ$  at  $25^\circ$  latitude. This agrees with the results of Tlatov et al. (2013). Therefore, we choose  $C_{\alpha\beta} = 0.5$  for the long-term runs of the model. Figure 2b shows the relation between the amplitude of the  $\alpha_\beta$  and the BMR’s tilt. The magnitude of tilt for the positive  $C_{\alpha\beta}$  is less than for the negative ones. This is likely because of the magnetic helicity effect which is contributed by the third term of the Eq(29). A detailed investigation of this effect is out of our scope.

We notice that the  $\alpha$  effect of the BMRs is readily linked with the tilt. The latitudinal dependence of this relationship is governed by the factor  $\cos \theta$ , see the Eq.(17).

Figure 3 shows snapshots of the axisymmetric magnetic, as well as distribution of the instability parameter  $I_\beta$  and results of calculation of the  $\alpha_\beta$  parameter for the distributions of the large-scale magnetic field. We take these snapshots at the growing phase of the magnetic cycle. In the southern hemisphere, the position of the dynamo wave is closer to the equator and the surface than in the northern hemisphere. The structure of the dynamo wave and the shallow instability effect ( $r_m > 0.85R$ , see comments below the Eq(15)) result in the difference in positions of the unstable points of the dynamo waves in the South and North hemispheres. The amplitude of the  $\alpha_\beta$  parameter is different as well. In the northern hemisphere, the magnitude of the  $\alpha_\beta$  is close to the maximum magnitude of the kinetic  $\alpha$  effect (cf, Fig4c).

We model the randomness of the tilt using the parameter  $\xi_\alpha$ . Similar to Rempel (2005), the  $\xi_\alpha$  evolution follows the Ornstein–Uhlenbeck process,

$$\begin{aligned} \dot{\xi}_\alpha &= -\frac{2}{\tau_\xi} (\xi_\alpha - \xi_1), \\ \dot{\xi}_1 &= -\frac{2}{\tau_\xi} (\xi_1 - \xi_2), \\ \dot{\xi}_2 &= -\frac{2}{\tau_\xi} \left( \xi_2 - g \sqrt{\frac{2\tau_\xi}{\tau_h}} \right). \end{aligned} \quad (18)$$

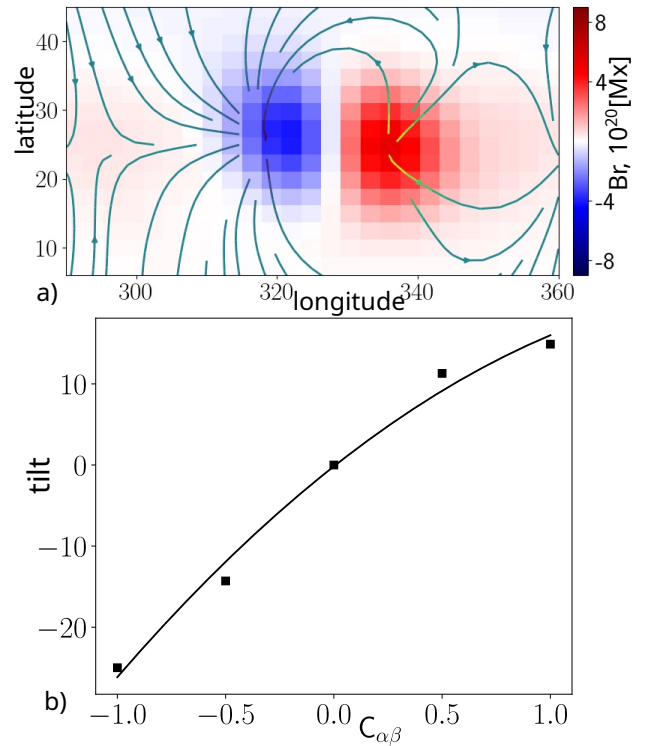


**Figure 2.** a) Snapshot of the bipolar group at the surface for  $C_\alpha = 1$ , the color image shows the flux of the radial magnetic field and streamlines show the surface components of the magnetic field; b) Relation of the BMRs tilt and the parameter  $C_{\alpha\beta}$  for the latitude  $25^\circ$ .

Here,  $g$  is a Gaussian random number. It is renewed every time step,  $\tau_h$ . The  $\tau_\xi$  is the relaxation time of  $\xi_\alpha$ . The parameters  $\xi_{1,2,3}$  are introduced to get a smooth variations of  $\xi_\alpha$ . Similar to the above cited papers, we choose the parameters of the Gaussian process as follows,  $\bar{g} = 0$ ,  $\sigma(g) = 1$  and  $\tau_\xi = 2$  months. Similar to the  $\xi_\beta$ , the parameter  $\xi_\alpha$  varies independently in the northern and southern hemispheres.

### 2.3 Basic parameters and boundary conditions

The model considers the effects of the large-scale magnetic field and flow on the axisymmetric mean-field heat transport and angular momentum balance in the solar convection zone. This part of the model was described earlier by Pipin (2017) and Pipin & Kosovichev (2020). Appendix B gives the basic equations governing the angular momentum balance and the meridional circulation. We use the MESA model (Paxton et al. 2011, 2013) to calculate the reference profiles of mean thermodynamic parameters, such as entropy, density, temperature and the convective turnover time,  $\tau_c$ . It assumes that  $\tau_c$  does not depend on evolution of the magnetic field and global flows. To define the convective RMS velocity  $u_c$  we use the mixing-length approximation,

$$u_c = \frac{\ell_c}{2} \sqrt{-\frac{g}{2c_p} \frac{\partial \bar{s}}{\partial r}}, \quad (19)$$

where  $\ell_c = \alpha_{MLT} H_p$  is the mixing length,  $\alpha_{MLT} = 1.9$  is the mixing length parameter, and  $H_p$  is the pressure height scale. The Eq. (19) defines the profiles of the eddy heat con-



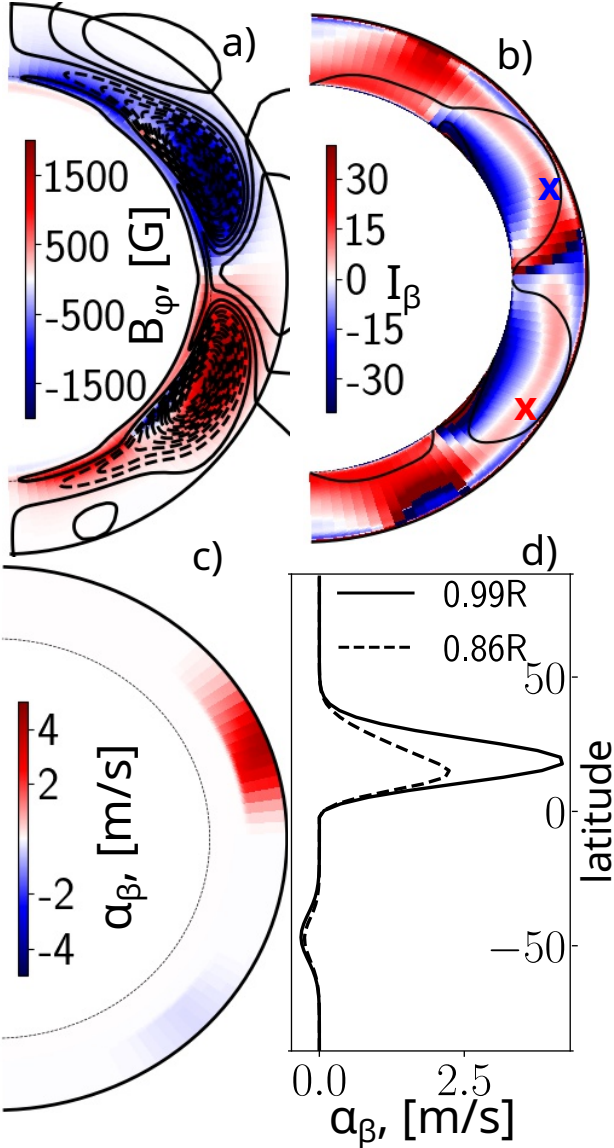


**Figure 3.** a) Snapshot of the axisymmetric magnetic field distribution for the growing phase of the magnetic cycle. The color shows the toroidal magnetic field strength, streamlines show the poloidal magnetic field; b) the snapshot of the instability parameter,  $I_\beta$ ; the red and blue crosses show locations of the unstable regions ( $I_\beta(r_m, \theta_m) > 0$ ,  $r_m > 0.85R$  and  $|\bar{B}_m| > 500\text{G}$ ) in the southern and northern hemispheres, respectively; c) the snapshot of the  $\alpha$  effect parameter,  $\alpha_\beta$ , for  $C_{\alpha\beta} = 0.5$  and  $\xi_\beta(r, \delta t = 5\tau_0)$ ; d) the latitudinal profiles of the  $\alpha_\beta$  at the bottom of the instability region (dashed line) and at the top (solid line).

ductivity,  $\chi_T$ , eddy viscosity,  $\nu_T$ , and eddy diffusivity,  $\eta_T$ , as follows,

$$\chi_T = \frac{\ell^2}{6} \sqrt{-\frac{g}{2c_p} \frac{\partial \bar{s}}{\partial r}}, \quad (20)$$

$$\nu_T = \text{Pr}_T \chi_T, \quad (21)$$

$$\eta_T = \text{Pm}_T \nu_T. \quad (22)$$

The mean entropy,  $\bar{s}$ , is determined from the mean-field heat transport equation. The model shows an agreement of the angular velocity profile with helioseismology results for  $\text{Pr}_T =$

**Table 1.** Basic parameters of the reference axisymmetric dynamo model (run X0, see Table 2) and the BMR's electromotive force

dynamo model parameters	BMR parameters
$C_\alpha = 0.042$ ,	emergence time, $\delta t = 5D$ ,
$\text{Pr}_T = 3/4, \text{Pm}_T = 10$ ,	growth rate $\tau_0 = 1D$ ,
$\beta^{CZ} \leq 0.2, V_m \sim 10^{-3}u_c$	$m_\beta = 100$ (BMR's size $\sim 10^\circ$ ),
	$V_\beta \sim e^{\delta t/\tau_0} V_m \sim 10\text{m/s}$ ,
	$ \alpha_\beta  = C_{\alpha\beta} V_\beta \sim 0 - 10\text{m/s}$

3/4. The dynamo cycle period of 22 years is reproduced if  $\text{Pm}_T = 10$  and  $C_\alpha = 0.042$ . The level  $C_\alpha$  is slightly above the critical threshold.

We divide the integration domain into two parts. The overshoot region includes the part of the radiative zone. We put the bottom of the integration domain at  $r_i = 0.68R$ . The convection zone extends from  $r_b = 0.728R$  to  $r_t = 0.99R$ . The solution of the heat transport gives the mean entropy distribution and determines the turbulent parameters in the convection zone. In the overshoot region, the intensity of the turbulent mixing decays exponentially from the bottom of the convection zone. The bottom boundary rotates as a solid body at the rate  $\Omega_0 = 430\text{NHz}$ . At the bottom we put the magnetic field induction vector to zero. At the top boundary, we use the black-body radiation heat flux and the stress-free condition for the hydrodynamic part of the problem.

For the dynamo problem, following ideas of Moss & Brandenburg (1992) and Pipin & Kosovichev (2011), we use the top boundary condition in the form that allows penetration of the toroidal magnetic field to the surface:

$$\delta \frac{\eta_T}{r_t} B \left( 1 + \left( \frac{|B|}{B_{\text{esq}}} \right) \right) + (1 - \delta) \mathcal{E}_\theta = 0, \quad (23)$$

where  $r_t = 0.99R$ . For the set of parameters  $\delta = 0.999$  and  $B_{\text{esq}} = 5\text{G}$  we get the surface toroidal field of magnitude around 1.5 G. This is in agreement with the results of the solar observations of Vidotto et al. (2018). The magnetic field potential outside the domain is

$$A^{(\text{vac})}(r, \mu) = \sum a_n \left( \frac{r_t}{r} \right)^n \sqrt{1 - \mu^2} P_n^1(\mu), \quad (24)$$

where  $\mu = \cos \theta$ . The nonaxisymmetric part of the dynamo model was solved using the spherical harmonics. For the numerical solution, we employ the FORTRAN version of the SHTNS library of Schaeffer (2013).

The Figure4 illustrates distributions of the angular velocity, meridional circulation, the  $\alpha$  - effect and the eddy diffusivity in the nonmagnetic case model. The amplitude of the meridional circulation on the surface is about 13 m/s. The angular velocity distribution is in agreement with the helioseismology data.

We list the basic parameters of our dynamo model in the Table1. The reference axisymmetric model is the same as in the paper of Pipin & Kosovichev (2020). The axisymmetric dynamo model operates in a weakly nonlinear regime with  $\beta^{CZ} \leq 0.2$ . In this case the maximum of the BMR's emergency velocity is about 10 m/s. This set a limit for the BMR's  $\alpha_\beta$  effect in our model. The fast-rotating solar analogs can have  $\beta^{CZ} \sim 1$  (see, Pipin 2021b). We can expect the larger magnitudes of  $V_\beta$  and  $\alpha_\beta$  for this case.

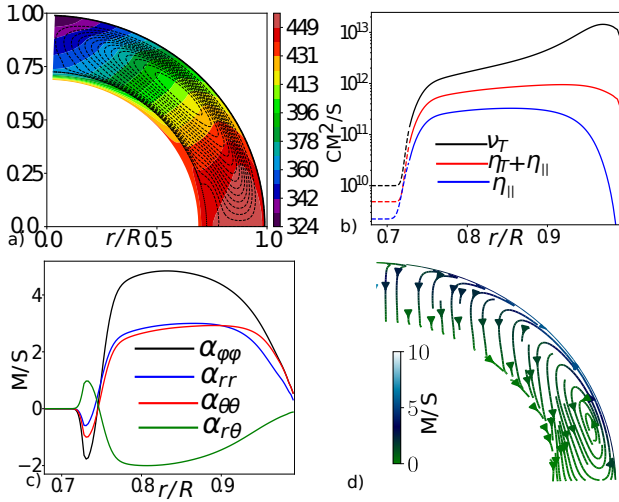


**Figure 4.** a) The meridional circulation (streamlines) and the angular velocity distributions; the magnitude of circulation velocity is of 13 m/s on the surface at the latitude of  $45^\circ$ ; b) radial dependencies of the total,  $\eta_T + \eta_{||}$ , and the rotationally induced part,  $\eta_{||}$ , of the eddy magnetic diffusivity and the eddy viscosity profile,  $\nu_T$ ; c) the  $\alpha$ -effect tensor distributions at the latitude of  $45^\circ$ ; and d) the streamlines of the toroidal magnetic field effective drift velocity because of the meridional circulation and the turbulent pumping effect. Here, and below we use `NUMPY/SCIPY` (Harris et al. 2020; Virtanen et al. 2020) together with `MATPLOTLIB` (Hunter 2007) and `PYVISTA` (Sullivan & Kaszynski 2019) for post-processing and visualization purposes.

**Table 2.** The parameters of the runs. The first three columns show the switches controlling the BMR's activity. The fourth column tells whether the nonaxisymmetric  $\alpha$  effect is included. The  $F_T$  is the magnitude of the total unsigned magnetic flux of the toroidal field in the convection zone;  $B_{\text{Pol}}$  is the strength of the polar magnetic field;  $P_{\text{cyc}}$  stands for the dynamo periods.

	$\xi_\beta$ , Eq.	$\xi_\alpha$ , Eq.	$C_{\alpha\beta}$	$\tilde{\alpha}_{ij}^{(H)}$ , Eq.	$F_T$ , [MX] $10^{24}$	$B_{\text{Pol}}$ , [G]	$P_{\text{cyc}}$ , yr
X0	0	0	0	0	$1.2 \pm 0.2$	18.6	11.2
X1	(14)	(18)	0.5	(7)	$1.3 \pm 0.15$	22.2	10.5
X2	(14)	0	0.	(7)	$1.3 \pm 0.15$	22.2	11.2
X3	(14)	0	0.5	(7)	$1.3 \pm 0.15$	22.2	10.5
X4	(14)	0	0.5	0	$1.2 \pm 0.1$	18.8	9

## 2.4 Diagnostic parameters

The Table 2 summarizes the control and integral dynamo parameters of the runs. In addition, we consider the following integral parameters of the magnetic activity: the magnitude of the total magnetic flux of the toroidal field in the convection zone,

$$F_T = 2\pi \int_{-1}^1 \int_{r_b}^{r_t} |\overline{B}_\phi| \sin \theta r^2 dr d\mu, \quad (25)$$

the strength of the polar magnetic field,

$$B_{\text{pol}} = \frac{1}{2} \left( \langle \overline{B}_r \rangle^{\theta < 20} - \langle \overline{B}_r \rangle^{\theta > 160} \right), \quad (26)$$

where  $\theta$  is the polar angle. We do the averaging of the radial magnetic field over the polar regions higher than  $70^\circ$  latitude. Also, we introduce the total flux of the unsigned radial magnetic field at the surface,

$$F_R = 2\pi R^2 \oint |\langle B_r \rangle| \sin \theta d\mu d\phi. \quad (27)$$

We characterize the hemispheric asymmetry of magnetic activity by the parity index (Knobloch et al. 1998). It defines as follows. As the first step, we calculate the parameters characterizing the energy of the symmetric and antisymmetric about the equator parts of the surface radial magnetic field:

$$E^{(e)} = \oint [\langle B_r \rangle(\mu, \phi, t) + \langle B_r \rangle(-\mu, \phi, t)]^2 d\mu d\phi,$$

$$E^{(o)} = \oint [\langle B_r \rangle(\mu, \phi, t) - \langle B_r \rangle(-\mu, \phi, t)]^2 d\mu d\phi.$$

Then, the parity index reads

$$P = \frac{E^{(e)} - E^{(o)}}{E^{(e)} + E^{(o)}}. \quad (28)$$

Below,  $\bar{P}$  and  $\tilde{P}$  stand for the parity parameter of the axisymmetric and nonaxisymmetric radial magnetic field, respectively. For the dipole type of the equatorial symmetry of the radial magnetic field, we get  $P = -1$ , and for the quadrupole type of the equatorial symmetry, we get  $P = 1$ . If the magnetic activity concentrates in one hemisphere, we have  $P \approx 0$ .

The emergence of the BMRs results in the excitation of the large-scale nonaxisymmetric magnetic field. This nonaxisymmetric magnetic field takes part in the large-scale dynamo as well. Considering the  $\alpha$  effect generation of the large-scale poloidal magnetic field via the azimuthal electromotive force, we can identify several contributions. The longitudinal averaging of the  $\alpha$  effect terms in  $\mathcal{E}_\phi$  results to

$$\mathcal{E}_\phi^{(\alpha)} = \overline{\alpha_{\phi\phi} \langle B \rangle_\phi} = \overline{\alpha_{\phi\phi} B} + \overline{\alpha_\beta \langle B \rangle_\phi} + \overline{\tilde{\alpha}_{\phi\phi} \tilde{B}_\phi}, \quad (29)$$

where the first term in the RHS is the standard part of the axisymmetric mean-field dynamos, the second term represents the effect of the BMRs or the Leighton effects (see, Leighton 1969). The third term results from the longitudinal averaging of the nonaxisymmetric part of the  $\alpha$  effect and the nonaxisymmetric magnetic field. It provides the coupling between the evolution of the axisymmetric and nonaxisymmetric magnetic fields (Bigazzi & Ruzmaikin 2004; Berdyugina et al. 2006). The  $\tilde{\alpha}_{\phi\phi}$  in the Eq(29) results from the nonlinear effects of the nonaxisymmetric magnetic fields on the kinetic and magnetic parts of the  $\alpha$  effect tensor in the Eq(7). In the run X3 we deliberately exclude  $\tilde{\alpha}_{\phi\phi}$  to see the impact of the BMR's  $\alpha$ -effect explicitly.

## 3 RESULTS

Figure 5 shows snapshots of the magnetic field distribution during the maximum of the magnetic cycle for model X1. At the low latitudes of the star, the magnetic field is fairly nonaxisymmetric in the shallow layer below the surface. The differential rotation stretches the toroidal field toward the poles

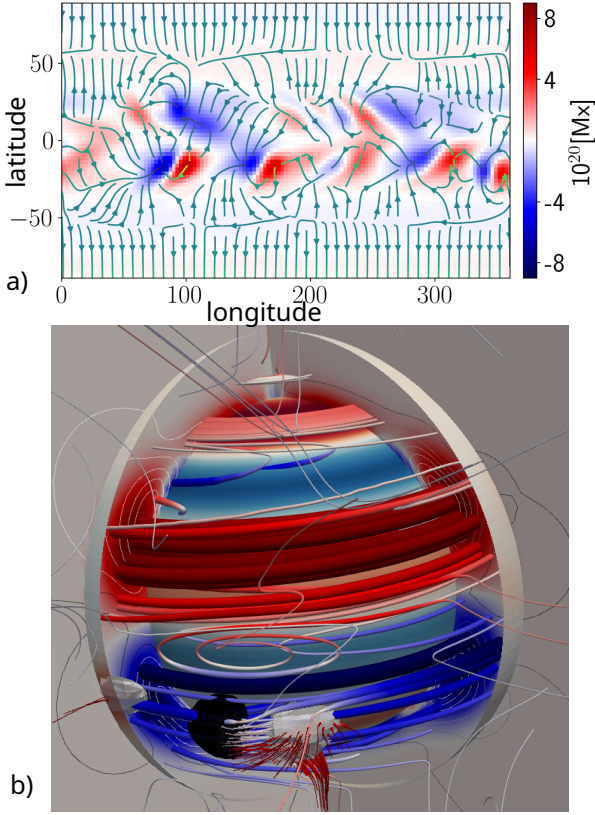


**Figure 5.** a) The snapshot of the surface radial magnetic flux distribution and streamlines of the surface magnetic field lines ( $\langle B \rangle_\theta, \langle B \rangle_\phi$ ); b) the snapshot of the magnetic field distributions inside the convection zone; the azimuth of the central meridian is equal to 0; the color image in the left and right segments and the inner sphere (bottom of the CZ) shows the toroidal magnetic field strength in the range of  $\pm 2\text{kG}$ ; contours in the left and right segments show the streamlines of the axisymmetric poloidal magnetic field; the magnetic field lines, which are colored by the gray; red and blue colors reflect the direction and the magnetic field strength (the white color means  $\langle B \rangle_\phi \approx 0$ ); the BMR is shown by islands which are colored in the black and white color; the islands confine the volumes of the radial magnetic field flux above the threshold of  $4 \cdot 10^{20}\text{Mx}$  per pixel.

from the nonaxisymmetric remnants of the large unipolar magnetic regions. The animated snapshots of the magnetic field evolution in run X1 are available online. We find that our model fairly well reproduces the evolution of the large-scale magnetic flux on the solar surface. The results are in qualitative agreement with solar observations (e.g., Giovanelli 1985; Wang et al. 1989; Virtanen et al. 2019; Mordvinov et al. 2022). The distribution of the magnetic field around the BMR is rather shallow (see, Fig5b). This is similar to the results of Miesch & Dikpati (2014).

### 3.1 The dynamo effects of BMRs

Figure 6 shows the time-latitude diagram of the axisymmetric magnetic field evolution in run X1. In the mid-latitudes, the radial magnetic field shows an intermittent surge-like pattern. It results from contributions of the weak diffuse field of the large-scale dynamo and remnants of the BMRs decay. A similar pattern is found in the surface flux transport models

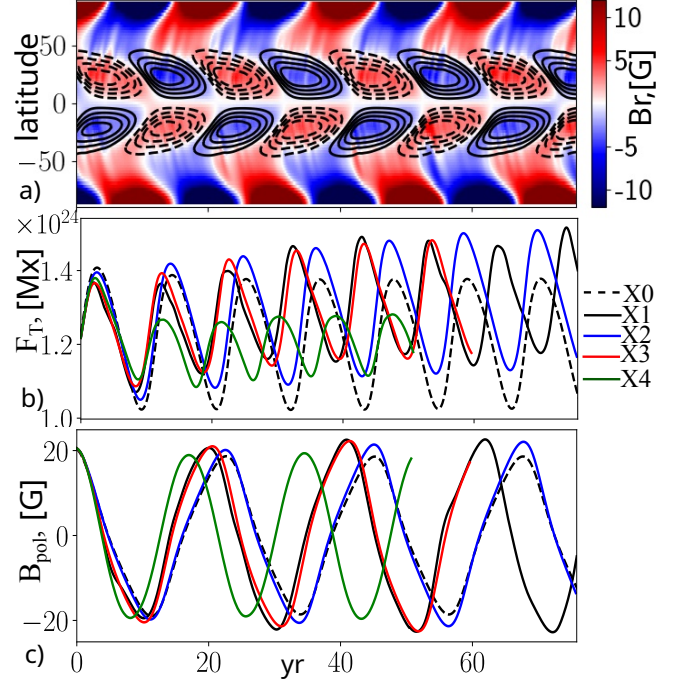


**Figure 6.** a) The time-latitude diagram of the surface radial magnetic field (color image) and the toroidal magnetic field at  $r=0.9R$  (contours in range of  $\pm 1\text{kG}$ ) in the run X1; b) the total flux of the axisymmetric toroidal magnetic field in the convection zone,  $F_T$ ; c) evolution of the polar magnetic field,  $B_{\text{pol}}$ .

and 3d Babcock-Leighton type models (e.g., Mackay & Yeates 2012; Hazra & Nandy 2019; Kumar et al. 2019). Also, the intermittent time-latitude pattern of the radial magnetic field evolution is a typical feature of any 2D dynamo model that includes the fluctuations of the  $\alpha$  effect (see, e.g., Yang et al. 2020; Pipin & Kosovichev 2020). The other 3D runs listed in Table 2, as well as the axisymmetric model X0, show the smooth time-latitude diagrams of the radial magnetic field (see, e.g., Pipin & Kosovichev 2019). In our description of the BMR formation, the BMR's tilt and  $\alpha$ -effect are readily connected. Therefore, the fluctuations of the BMR's  $\alpha$  effect result in violations of the Joy law. Our results agree with the conclusions of Mordvinov et al. (2022) who showed that the intermittency of the radial magnetic field evolution on the surface likely results from violations of Hale's and Joy's laws in emerging BMRs.

Starting our simulations from the same initial conditions, we compare the integral dynamo parameters of the runs. Figures 6b and c show the toroidal flux parameter  $F_T$  and the polar magnetic field,  $B_{\text{pol}}$ , see the Eqs. (25) and (26). All 3D runs, except the run X4 show a higher magnitude of the  $F_T$  and  $B_{\text{pol}}$  parameters than the run X0. The runs X2 and X0 show a longer dynamo period than the runs X1, X3, and X4. Interesting that the run X4, where we neglect the mean-field  $\alpha$ -effect of the nonaxisymmetric magnetic field, shows the smallest magnitude of the  $F_T$  parameter and the shortest dynamo period. These simulations show the importance of the mean-field  $\alpha$ -effect in the dynamo evolution of the nonaxisymmetric magnetic field. Noteworthy, the Babcock-Leighton solar dynamo models usually ignore the mean-field  $\alpha$  effect acting on the nonaxisymmetric magnetic fields (terms



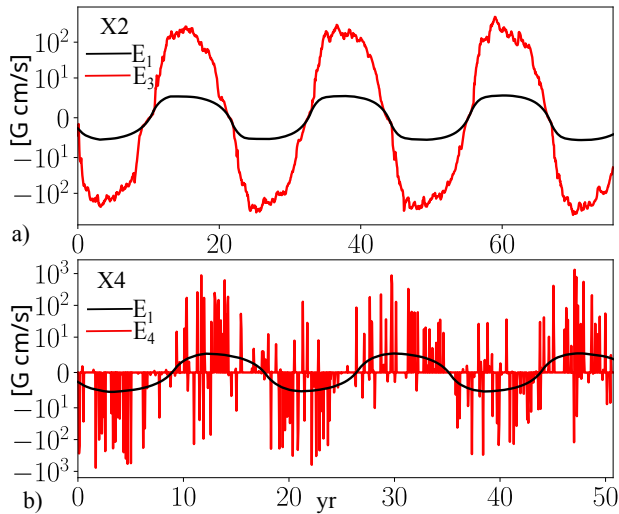


**Figure 7.** The mean electromotive force of the  $\alpha$  effect at the surface:  $E_1$  - the  $\alpha$  effect of the axisymmetric toroidal field;  $E_3$  the  $\alpha$  effect of the nonaxisymmetric toroidal field;  $E_4$  - the  $\alpha$  effect due to the BMR's tilt. a) the run X2; b) the same for the run X4.

like  $\overline{\tilde{\alpha}_{\phi\phi}\tilde{B}_{\phi}}$  in the Eq(29)). We find that the model X2, which has  $\alpha_{\beta} = 0$ , shows a higher dynamo efficiency than the other 3D runs.

The azimuthal part of the mean electromotive force, which results in the dynamo generation of the axisymmetric poloidal magnetic field by the  $\alpha$  effect, reads,

$$\begin{aligned} \mathcal{E}_{\phi}^{\alpha} &= \left( \overline{\alpha}^{(H)} + \overline{\alpha}^{(M)} \right) B + \overline{\tilde{\alpha}_{\phi\phi}\tilde{B}_{\phi}} + \overline{\alpha_{\beta}(B)_{\phi}}, \quad (30) \\ &\equiv E_1 + E_2 + E_3 + E_4 \quad (31) \end{aligned}$$

where the terms  $E_{\{n\}}$  denote the corresponding terms in the Eq(30), e.g.,  $E_2 \equiv \overline{\alpha}^{(M)} B$ . We are interested to compare the efficiency of the magnetic field generation by means  $E_3$  and  $E_4$ . Also, we have to remember that the mean field generation term  $E_3$  includes the magnetic helicity effect (see, the Eq(7)). Figure 7 shows the time series of  $E_{1,3,4}$  for the runs X2 and X4 at the surface. Note that we have  $E_4 = 0$  in the run X2 and  $E_3 = 0$  in the run X4. The run X2 shows  $E_3 \geq E_1$ . It is due to  $|\tilde{B}_{\phi}| > |\overline{B}_{\phi}|$  at the top because of the boundary conditions ( $|\overline{B}_{\phi}| \sim 1G$ ). The run X4 shows the same. However, the mean variation of the  $E_3$  in the run X2 shows the greater magnitude than the mean variation of the  $E_4$  in the run X4. Because the action of the  $\alpha_{\beta}$  is limited by the emerging time of the BMRs. The fluctuations of the time series  $E_3$  and  $E_4$  in the models X2 and X4 are because of the random emergence of the BMRs at the surface and the magnetic helicity effect.

Figure 8a shows the evolution of the unsigned surface radial magnetic field flux,  $F_R$ . In the run X1, the flux correlates with the activity of the near-surface toroidal magnetic field (cf, Fig6a). We find the same in other 3D runs. This agrees with the solar observations. Stenflo (2013) found the unsigned surface radial magnetic field flux to be a good proxy for the sunspot activity. The runs X1 and X3, which include the  $\alpha_{\beta}$  effect, show the higher magnitude of the  $F_R$  than the other 3D runs. These runs show the increase of the baseline of the  $F_R$  as well. The run X4 shows the lowest baseline of the  $F_R$ . In this run, we neglected the mean-field  $\alpha$  effect for

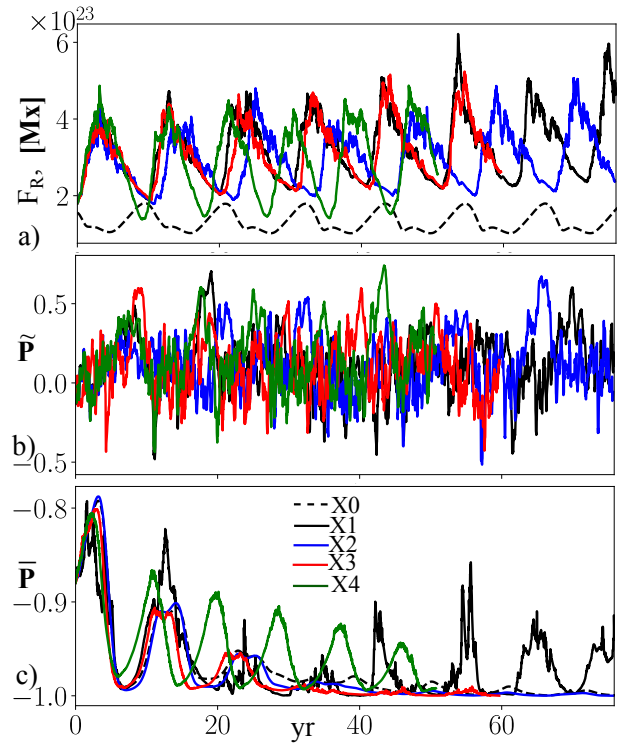


**Figure 8.** a) The total unsigned surface radial magnetic field flux,  $F_R$ ; b) the parity parameter for the nonaxisymmetric radial magnetic field,  $\tilde{P}$ , (see, the Eq(28)); c) the same as b) for the parity parameter of the axisymmetric radial magnetic field,  $\bar{P}$ . The line notation is the same as in Fig6.

the nonaxisymmetric magnetic field. We conclude that the runs X1-X3 show the dynamo instability of the nonaxisymmetric magnetic field. This instability is excited due to the emergence of the BMRs at the top of the dynamo domain. The run X2 is the interesting case of the dynamo model run where we neglect the BMR's tilt, putting  $\alpha_{\beta} = 0$ . Still, in the run X2, the emerging BMRs satisfy, by construction, the Hale polarity rule. Our results show that, in this case, the mean-field  $\alpha$  effect supports the dynamo generation of the axisymmetric poloidal magnetic field, and it contributes to the nonaxisymmetric dynamo, as well.

### 3.2 The dynamo parity breaking

Figs.8 b and c show evolution of the parity parameters,  $\tilde{P}$  and  $\bar{P}$ . These parameters characterize the equatorial symmetry of the magnetic activity. The parity of the nonaxisymmetric magnetic field,  $\tilde{P}$ , varies around zero. In the 3D runs the zero magnitude of  $\tilde{P}$  correlates approximately with epochs of the magnetic activity maximum, which corresponds to the maxima of the  $F_R$  parameter. The maximum magnitude of the  $\tilde{P}$  (of either positive or negative signs) correlates approximately with minima of the  $F_R$ . The parameter  $\bar{P}$  shows variations around  $-1$ , where  $\bar{P} = -1$  corresponds to the minimum of the magnetic cycle. In whole, the 3D runs show the highest hemispheric asymmetry of the magnetic activity for epochs of the magnetic cycle maximum. The run X1 shows the highest hemispheric asymmetry of magnetic activity among our runs.

In our model, the initial magnetic field has a mix of the



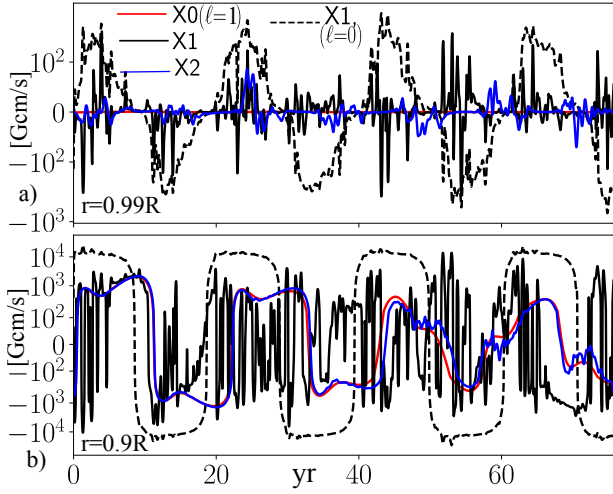


**Figure 9.** a) Evolution of the first three *even* harmonics,  $\ell_0$  (black solid line),  $\ell_2$  (red line),  $\ell_4$  (blue line) and the odd harmonic  $\ell_1$  (black dashed line) of the  $\mathcal{E}_\phi^\alpha$  (see the Eq(30)) at the near surface level  $r=0.987R$ ; b) the same as a) for  $r=0.86R$ .

dipole and quadrupole parities magnetic fields and the dipole type magnetic field dominates. We choose the  $C_\alpha$  parameter about of 10 percent above the dynamo threshold. For this case, the quadrupole modes of the dynamo solution are below the dynamo instability threshold. Fig8c shows the slow decay of the quadrupole modes in the run X0 with time, as the parameter  $\bar{P}$  approaches to  $-1$ . The run X1 shows that the fluctuations of the  $\alpha_\beta$  can support the generation of the quadrupole mode of the large-scale magnetic field. To shed some light at this phenomenon, we consider the spherical harmonic decomposition for the mean electromotive force. The modes  $\ell = 0$  and  $\ell = 1$  of the  $\mathcal{E}_\phi^{(\alpha)}$  (see, the Eq29) generate the dipole and quadrupole modes of the radial magnetic field, respectively. The Fig9 shows evolution of the modes  $\ell = 0$  and  $\ell = 1$  of the  $\mathcal{E}_\phi^{(\alpha)}$  for the two levels of the convection zone and three dynamo runs, X0, X1, and X2. The  $\ell = 0$  mode of the  $\mathcal{E}_\phi^{(\alpha)}$  shows the stable oscillations of nearly the same magnitude in all the runs. In the run X1 (with fluctuations of the BMR's tilt), the mode  $\ell = 1$  of the  $\mathcal{E}_\phi^{(\alpha)}$  shows the stable oscillations both at the surface and inside the convection zone. In the run X2 there are small fluctuations of the mode  $\ell = 1$  of the  $\mathcal{E}_\phi^{(\alpha)}$  at the surface. They are because of the magnetic helicity effect and the random emergence of the BMRs. Inside the convection zone, the run X2 shows a slow decay of the  $\ell = 1$  mode. Its evolution follows the run X0.

### 3.3 Magnetic helicity evolution

Figure 10 shows the synoptic map of the surface magnetic field and magnetic helicity density distribution for the run X1 for the epoch of the magnetic activity maximum (a month before the snapshot, which is shown in Fig5). Similar to the results of Yeates (2020); Pipin (2021a), we find that the emergence of the BMR in the ambient large-scale field injects the magnetic helicity at the same place. The effect results from the magnetic helicity conservation.

From Fig.10b we see that the new active region, which is at about 20 longitudes in the southern hemisphere, shows the quadrupole helicity density pattern. The evolution of the

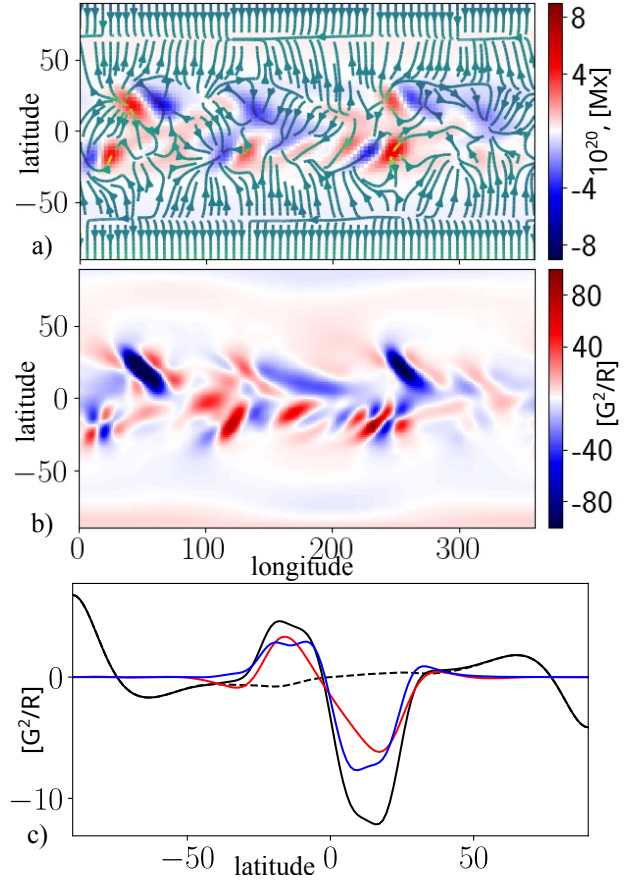


**Figure 10.** a) Snapshot of the density flux of the radial magnetic field (color image) and streamlines of the surface magnetic field (color image with streamlines); b) the snapshot of the magnetic helicity density; c) the longitudinally averaged magnetic helicity density: black solid line shows the total magnetic helicity density  $\langle \mathbf{A} \cdot \langle \mathbf{B} \rangle$ , the dashed line shows  $\bar{\mathbf{A}} \cdot \bar{\mathbf{B}}$ , the red line shows  $-\bar{A}_\phi \bar{B}_\phi$ , and the blue line shows  $-\bar{A}_\theta \bar{B}_\theta$ .

emerging BMR involves the  $\alpha$ -effect acting on the azimuthal magnetic field surrounding the BMR and the effect of the differential rotation. Because of the magnetic helicity conservation, the generated helicity density has the sign which is opposite to the sign of the  $\alpha$ -effect. This explains why the developed BMRs in the southern hemisphere show a preference for the positive helicity density inside the BMRs. The opposite happens in the northern hemisphere.

Because of the total helicity balance, the effect of the injected BMRs helicity is small. The polar sides of the synoptic maps show the large-scale field helicity density satisfies the hemispheric sign rule, i.e., it has a positive sign in the northern hemisphere. The results of the longitudinal average of the synoptic map Fig10b is shown in Fig10c. In each hemisphere, the imbalance of the total helicity is more than an order of magnitude less than those extrema in Fig10c.

Fig.11 shows results of the model for the time-latitude evolution of the toroidal magnetic field in the subsurface layer and the magnetic helicity evolution. The results for the total magnetic helicity (Fig. 11a) are in qualitative agreement with the solar observation (see, e.g., Lund et al. 2020 and Pevtsov et al. 2021). The evolution of the small-scale helicity density,  $\langle \chi \rangle$ , which is produced by the dynamo, follows the Eq(8). The

model shows the surface  $\langle \chi \rangle$  time-latitude diagram in agreement with the results of our previous papers and we do not show it here (see, e.g. Pipin et al. 2013; Pipin 2018). Instead, the rather interesting question is about the helicity density evolution of the large-scale nonaxisymmetric magnetic field. Fig.11b show the time-latitude evolution of the  $\bar{\mathbf{A}} \cdot \bar{\mathbf{B}}$  and similar diagram for the axisymmetric magnetic field helicity density, i.e.,  $\bar{\mathbf{A}} \cdot \bar{\mathbf{B}}$ . The  $\bar{\mathbf{A}} \cdot \bar{\mathbf{B}}$  show the good agreement with the results of Pipin et al. (2019), who measured the helicity density using the synoptic maps of SDO/HMI. We see that the helicity density  $\bar{\mathbf{A}} \cdot \bar{\mathbf{B}}$  shows the predominantly negative sign in the northern hemisphere and opposite sign in the southern hemisphere. This agrees with the hemispheric sign rule (HSR) for the current helicity of the solar active regions (Seehafer 1990; Pevtsov et al. 1994; Bao et al. 2000; Zhang et al. 2010). The magnetic field, which is involved in the  $\bar{\mathbf{A}} \cdot \bar{\mathbf{B}}$  occupies the intermediate spatial scales. On the surface, the axisymmetric magnetic field shows variations of the helicity density sign from the negative in the northern hemisphere during the minimum of the magnetic cycle to the positive during the maximum cycle. In the southern hemisphere, the  $\bar{\mathbf{A}} \cdot \bar{\mathbf{B}}$  evolves oppositely. A very similar pattern is found in the solar observations (Pevtsov et al. 2021).

The theoretical expectation suggests the bi-helical magnetic field in the large-scale dynamo (Blackman & Brandenburg (2003); Brandenburg (2018); Brandenburg et al. (2017a)). The direct computation of the helicity spectrum from distributions of the vector-potential and magnetic field has two issues. It depends on the gauge of the vector potential. Another issue is that the different  $\ell$  harmonics of the magnetic helicity density may not show the same hemispheric sign rule. The two-scale approach of Roberts & Soward (1975) was suggested and developed (see, Brandenburg et al. (2017a); Brandenburg (2019)) to overcome the issues. On the first try, we calculate the helicity proxy spectrum suggested by Brandenburg (2019). The proxy is determined by the spherical harmonics of the superpotentials S and T (see, 4) as follows

$$H_{\ell}^{\pm} = \sum_{m=-\ell}^{m=\ell} 2\ell(\ell+1) S_{\ell m} T_{\ell \pm 1 m}^*, \quad (32)$$

where the shift  $\ell \pm 1$  was introduced to account for the two-scale approximation. By definition, the  $H_{\ell}^{\pm}$  should have the positive sign at the low  $\ell$  in correspondence of the conventional hemispheric sign rule, i.e., the predominantly positive helicity for the large-scale magnetic field in the northern hemisphere. Fig.11c and d show the evolution of the  $H_{\ell}^+$  at the surface for the axisymmetric and nonaxisymmetric parts of the surface magnetic field. The general sign of  $H_{\ell}^+$  agrees with the helicity density evolution shown in Figs.11a and b. The  $\ell_1$  mode shows the positive sign in agreement with the large-scale helicity density on the synoptic maps of Fig.10.

Contrary to the theoretical expectations (see, e.g. Brandenburg et al. 2017a), we see that  $H_{\ell}^+$  of the axisymmetric magnetic field shows the positive sign during the maximum cycle only for the dipole modes. The octupole modes show the negative sign of  $H_{\ell}^+$ . Also, the large-scale nonaxisymmetric field shows a tendency for the positive helicity sign of  $H_{\ell}^+$  in the low modes  $\ell = 1 - 5$  during epochs of the mag-

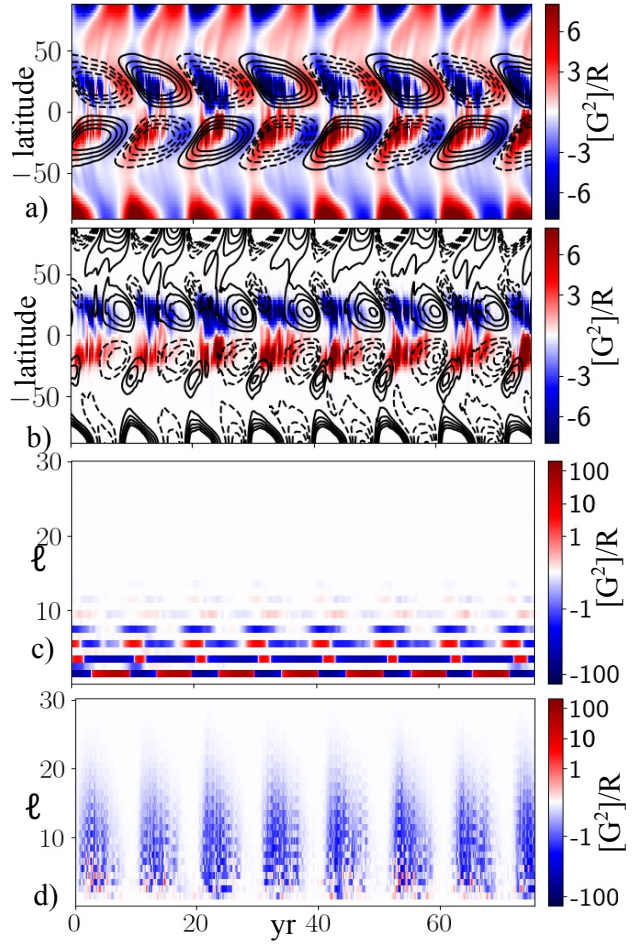


**Figure 11.** a) The time-latitude diagram of the total magnetic helicity of the large-scale field (color image), contours  $\pm 1\text{kG}$  show the toroidal magnetic field in the subsurface layer  $r=0.9R$ ; b) the color image shows the magnetic helicity density of the nonaxisymmetric magnetic field, and contours show the same (in the same range) for the axisymmetric magnetic field; c) the helicity proxy spectrum,  $H_{\ell}^+$  (see, the Eq.32) evolution of the axisymmetric magnetic field at the surface; d) the same as c) for the nonaxisymmetric magnetic field.

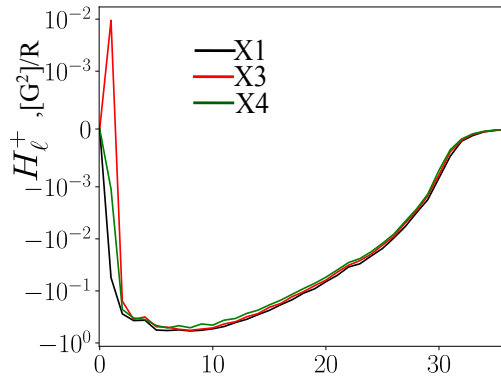


**Figure 12.** The time averaged spectrum  $H_{\ell}^+$  as computed from the nonaxisymmetric magnetic field for the runs X1, X3 and X4.

netic cycle maxima. The sign inversions of  $H_\ell^+$  during those periods of time are present as well. Such a fluctuating behavior of the bihelical spectrum seems to be typical for the solar magnetic field (Brandenburg et al. 2017a; Brandenburg 2019; Prabhu et al. 2021). In almost all run the bihelical feature of  $H_\ell^+$  disappear after the averaging of the time series. This is illustrated by Fig12. Yet, the run X3, which excludes variations of the BMR's tilt, show  $H_\ell^+ > 0$  for  $\ell = 2$  after time averaging. This proves an important role of the BMR's tilt in the bihelical spectrum of the large-scale nonaxisymmetric magnetic field of the solar type dynamos.

#### 4 DISCUSSION AND CONCLUSIONS

The dynamo model, which is presented in the paper, combines the framework of the mean-field dynamo and phenomenological parts of the Babcock-Leighton scenarios. The parameters of the mean-field part of our model, such as the  $\alpha$  effect and the eddy diffusivity profiles, are the same in the axisymmetric and nonaxisymmetric parts of the model. We calibrate these parameters on the solar observations using the reference 2D dynamo model. The reference dynamo model reproduces the basic properties of the solar magnetic activity cycle, such as the dynamo cycle period, the time latitude diagrams of the radial magnetic field evolution. In addition, the axisymmetric dynamo model consistently reproduces the solar-like angular velocity and meridional circulation profiles of the solar convection zone and their solar cycle variations (Pipin & Kosovichev 2020; Getling et al. 2021). The emerging BMRs affect the solar cycle variations of the angular velocity and the meridional circulation (Komm et al. (2015); Howe et al. (2018); Kosovichev & Pipin (2019); Getling et al. (2021)). We postpone the discussion of these effects to another paper.

The model adopts the Babcock-Leighton scenario using the well-known effects of the mean electromotive force. The BMR is generated through the magnetic buoyancy effect. The  $\alpha_\beta$  effect introduces the tilt of the BMR. We chose the parameters of the phenomenological part of the model to fit roughly the parameters of the solar BMRs. In particular, we show the direct relation of the  $\alpha_\beta$  effect (see, the Eq11) and the BMR's tilt. Besides the  $\alpha_\beta$  effect, the model of the BMR's formation includes a lot of free parameters which control the temporal and spatial characteristics of the BMR's formation. We did not study the effects of the BMR's formation parameters on the dynamo evolution in detail.

Compared to the Babcock-Leighton dynamos (e.g., Mackay & Yeates 2012; Miesch & Dikpati 2014; Kumar et al. 2019), the effect of the surface magnetic activity on the dynamo in the convection zone is not strong. The reason is that because the nonaxisymmetric magnetic field, which is generated from the evolution of the BMRs, is shallow. For given parameters, the dynamo runs reproduce the total surface radial magnetic field flux in agreement with observations by an order of magnitude. The approximate budget of the surface magnetic flux of the radial magnetic field in our models is of magnitude  $F_R \sim 5 - 7 \cdot 10^{23}$  Mx during the magnetic cycle maximum. Most of this flux is originated from the emergence and evolution of the BMRs. Comparing the 3D runs with the axisymmetric dynamo model, we find that this level of the BMR's activity results in about of 10 percent increase

of the total toroidal magnetic field flux in the convection zone. In the Babcock-Leighton dynamo models, the tilt of the BMRs is often considered as the key ingredient for the generation of the large-scale poloidal magnetic field (see, the above cited paper). Also, the flux-transport dynamo models ignore the background  $\alpha$  effect, which can act on the nonaxisymmetric magnetic field of the BMRs. We find this mechanism has a more profound effect on generation of the large-scale poloidal magnetic field than the BMR's tilt. Therefore, the role of Joy's law in our dynamo model differs from the pure Babcock-Leighton or flux-transport dynamo models.

In our model, instead of Joy's law itself, its fluctuations seem to be rather important. They result in the surge-like pattern of the poloidal magnetic field evolution on the solar surface. Also, such fluctuations result in the dynamo parity breaking and the hemispheric asymmetry of the magnetic activity. Hazra & Nandy (2019) discussed recently in the problem of the long-term parity variations of the solar magnetic activity. For given dynamo parameters, the axisymmetric dynamo model shows the decay of the quadrupole modes of the magnetic field. I find the same for the 3D models that have the fixed BMR's tilt. Interesting that the fluctuation part of the mean electromotive force, which generates the quadrupole component of the radial magnetic field, penetrates deep in the convection zone. Therefore, the surface effect of the tilt fluctuations of the BMRs results in the global dynamo excitation of the quadrupole-like magnetic field.

The model allows us to study the effects of the BMR on the surface magnetic helicity evolution. This is important both for interpretation of the solar observation and understanding the origin of the helicity of the solar magnetic field. The emerged BMRs result in surface helicity density distributions with nearly zero integral imbalance (Yeates 2020). Therefore, the magnetic part of the  $\alpha$  effect of these BMRs on the large-scale dynamo is about zero. The results in Fig11 show that on the surface, the effects of the helicity contributions, which come from the large-scale dynamo, are contaminated by the helicity injection because of the BMR emergence. The model shows that the hemispheric sign rule of the large-scale nonaxisymmetric magnetic field helicity density corresponds to the expected sign rule of the small-scale magnetic field helicity density, i.e., the  $\overline{\mathbf{A}} \cdot \overline{\mathbf{B}}$  has the negative sign in the northern hemisphere.

We use the proxy parameter suggested by Brandenburg (2019) to investigate the dynamo properties of the magnetic helicity spectrum. Indeed, the proxy shows the bihelical spectrum (see, Figs11c and d) with a positive helicity sign for the low  $\ell$  modes. The rest of the spectrum shows the negative helicity sign. Interesting, that the nonaxisymmetric magnetic field shows a tendency for the bihelical spectrum during the maximum of the magnetic cycles. This tendency is rather noisy. The solar observations (see, the above cited papers) show similar behavior. From a theoretical point of view the bihelical spectrum of the nonaxisymmetric magnetic field is evidence in favor of the large-scale nonaxisymmetric dynamo. It is indeed present in the 3D runs. In our models this dynamo is stochastic by nature. It is excited by the BMRs activity at the top of the dynamo domain. Our results shows that the BMR's tilt seems to be important for this stochastic dynamo.

In the above discussion, we mentioned that in our model, the dynamo efficiency of the surface BMRs activity is not strong. Yet, the 2D dynamo models which neglect this effect



can not explain directly the magnitude of the surface magnetic flux produced by the solar dynamo. The dynamo model operates in a weakly nonlinear regime with the toroidal magnetic field strength  $|\overline{B}| < 0.2B_{eq}$ , where  $B_{eq}$  is the equipartition magnetic field strength. For young solar analogs which are rotating with a period of 10 days and less, we expect  $|\overline{B}| \geq B_{eq}$ . In this situation, the BMR's production by the magnetic buoyancy can become much more efficient than for the modern Sun. Therefore, the surface BMRs activity can be crucial for the solar-type dynamo in the fast-rotating stars. The additional dynamo effects, which stem from the BMRs activity, can decrease the dynamo period (runs X1, X3 and X4). Therefore, this mechanism can be important in understanding the puzzling behavior of the dynamo period for the "quiet" activity branch of fast-rotating solar analogs (see, [Brandenburg et al. 2017b](#)).

Finally, I would like to summarize the major results of the study as follows. We investigate the effect of the tilted bipolar magnetic regions (BMR) emergence on the large-scale dynamo distributed in the bulk of the convection zone. Our results show that bipolar active regions make a meaningful addition to the dynamo generation of the large-scale poloidal magnetic field of the Sun. The mean-field  $\alpha$  effect, which acts on the nonaxisymmetric magnetic field of the BMRs, provides a greater contribution to the dynamo process than the BMR's tilt does. The fluctuations of the BMR's tilt lead to the parity braking in the global dynamo. In addition, the helicity density of the nonaxisymmetric magnetic field of the BMRs shows the hemispheric polarity rule, having the negative sign in the northern hemisphere of the Sun. Therefore, the dynamo activity of the surface BMRs seems to control the intermediate scales of the helicity spectrum of the solar magnetic field at the photosphere.

#### Acknowledgements

This work was carried out within the framework of the international team project leading by F.A. Pevtsov on Reconstruction of the evolution of the magnetic field of the Sun and the heliosphere over the past century with the support of the International Space Science Institute (ISSI), Bern, Switzerland. Also, the author thanks the financial support of the Ministry of Science and Higher Education of the Russian Federation (Subsidy No.075-GZ/C3569/278).

**Data Availability Statements.** The data underlying this article are available by request.

#### REFERENCES

Babcock H. W., 1961, [ApJ](#), **133**, 572  
 Bao S. D., Ai G. X., Zhang H. Q., 2000, [Journal of Astrophysics and Astronomy](#), **21**, 303  
 Berdyugina S. V., Moss D., Sokoloff D., Usoskin I. G., 2006, [A&A](#), **445**, 703  
 Berger M. A., Hornig G., 2018, [Journal of Physics A Mathematical General](#), **51**, 495501  
 Bigazzi A., Ruzmaikin A., 2004, [ApJ](#), **604**, 944  
 Blackman E. G., Brandenburg A., 2003, [ApJ](#), **584**, L99  
 Bonanno A., 2016, [ApJ](#), **833**, L22  
 Brandenburg A., 2018, [Journal of Plasma Physics](#), **84**, 735840404  
 Brandenburg A., 2019, [ApJ](#), **883**, 119  
 Brandenburg A., Kleorin N., Rogachevskii I., 2013, [ApJ](#), **776**, L23  
 Brandenburg A., Petrie G. J. D., Singh N. K., 2017a, [ApJ](#), **836**, 21  
 Brandenburg A., Mathur S., Metcalfe T. S., 2017b, [ApJ](#), **845**, 79

Brun A., Garcia R., Houdek G., Nandy D., Pinsonneault M., 2014, [Space Science Reviews](#), pp 1–54  
 Cameron R. H., Schüssler M., 2017, [A&A](#), **599**, A52  
 Getling A. V., 2001, [Astronomy Reports](#), **45**, 569  
 Getling A. V., Kosovichev A. G., Zhao J., 2021, [ApJ](#), **908**, L50  
 Gilman P. A., 1970, [ApJ](#), **162**, 1019  
 Gilman P. A., 2018, [ApJ](#), **867**, 45  
 Giovanelli R. G., 1985, [Australian Journal of Physics](#), **38**, 1045  
 Harris C. R., et al., 2020, [Nature](#), **585**, 357  
 Hazra S., Nandy D., 2019, [MNRAS](#), **489**, 4329  
 Howe R., Hill F., Komm R., Chaplin W. J., Elsworth Y., Davies G. R., Schou J., Thompson M. J., 2018, [ApJ](#), **862**, L5  
 Hubbard A., Brandenburg A., 2012, [ApJ](#), **748**, 51  
 Hunter J. D., 2007, [Computing in Science & Engineering](#), **9**, 90  
 Karak B. B., Jiang J., Miesch M. S., Charbonneau P., Choudhuri A. R., 2014, [Space Sci. Rev.](#), **186**, 561  
 Kitchatinov L. L., Mazur M. V., 2000, [Sol. Phys.](#), **191**, 325  
 Kitchatinov L. L., Pipin V. V., 1993, [A&A](#), **274**, 647  
 Kitchatinov L. L., Rüdiger G., 1992, [A&A](#), **260**, 494  
 Kitchatinov L. L., Pipin V. V., Ruediger G., 1994, [Astronomische Nachrichten](#), **315**, 157  
 Kleorin N., Rogachevskii I., 1999, [Phys. Rev.E](#), **59**, 6724  
 Kleorin N. I., Rogachevskii I. V., Ruzmaikin A. A., 1989, [Pis ma Astronomicheskii Zhurnal](#), **15**, 639  
 Kleorin N., Safiullin N., Kuzanyan K., Rogachevskii I., Tlatov A., Porshnev S., 2020, [MNRAS](#), **495**, 238  
 Knobloch E., Tobias S. M., Weiss N. O., 1998, [MNRAS](#), **297**, 1123  
 Komm R., González Hernández I., Howe R., Hill F., 2015, [Sol. Phys.](#), **290**, 3113  
 Kosovichev A. G., Pipin V. V., 2019, [ApJ](#), **871**, L20  
 Krause F., Rädler K.-H., 1980, [Mean-Field Magnetohydrodynamics and Dynamo Theory](#). Berlin: Akademie-Verlag  
 Kumar R., Jouve L., Nandy D., 2019, [A&A](#), **623**, A54  
 Leighton R. B., 1964, [ApJ](#), **140**, 1547  
 Leighton R. B., 1969, [ApJ](#), **156**, 1  
 Losada I. R., Warnecke J., Glogowski K., Roth M., Brandenburg A., Kleorin N., Rogachevskii I., 2017, in Vargas Domínguez S., Kosovichev A. G., Antolin P., Harra L., eds, [IAU Symposium Vol. 327, Fine Structure and Dynamics of the Solar Atmosphere](#). pp 46–59 ([arXiv:1704.04062](#)), [doi:10.1017/S1743921317004306](#)  
 Lund K., et al., 2020, [MNRAS](#), **493**, 1003  
 Mackay D. H., Yeates A. R., 2012, [Living Reviews in Solar Physics](#), **9**, 6  
 Miesch M. S., Dikpati M., 2014, [ApJ](#), **785**, L8  
 Mitra D., Candelaresi S., Chatterjee P., Tavakol R., Brandenburg A., 2010, [Astronomische Nachrichten](#), **331**, 130  
 Moffatt H. K., 1978, [Magnetic Field Generation in Electrically Conducting Fluids](#). Cambridge, England: Cambridge University Press  
 Mordvinov A. V., Karak B. B., Banerjee D., Golubeva E. M., Khlystova A. I., Zhukova A. V., Kumar P., 2022, [MNRAS](#), **510**, 1331  
 Moss D., Brandenburg A., 1992, [A&A](#), **256**, 371  
 Moss D., Tuominen I., Brandenburg A., 1991, [A&A](#), **245**, 129  
 Parker E. N., 1979, [Cosmical magnetic fields: Their origin and their activity](#). Oxford: Clarendon Press  
 Passos D., Nandy D., Hazra S., Lopes I., 2014, [A&A](#), **563**, A18  
 Paxton B., Bildsten L., Dotter A., Herwig F., Lesaffre P., Timmes F., 2011, [ApJS](#), **192**, 3  
 Paxton B., et al., 2013, [ApJS](#), **208**, 4  
 Petrie G. J. D., Petrovay K., Schatten K., 2014, [Space Sci. Rev.](#), **186**, 325  
 Pevtsov A. A., Canfield R. C., Metcalf T. R., 1994, [ApJ](#), **425**, L117  
 Pevtsov A. A., Bertello L., Nagovitsyn Y. A., Tlatov A. G., Pipin V. V., 2021, [Journal of Space Weather and Space Climate](#), **11**, 4



- Pipin V. V., 2008, *Geophysical and Astrophysical Fluid Dynamics*, **102**, 21
- Pipin V. V., 2017, *MNRAS*, **466**, 3007
- Pipin V. V., 2018, *Journal of Atmospheric and Solar-Terrestrial Physics*, **179**, 185
- Pipin V. V., 2021a, *Journal of Plasma Physics*, **87**, 775870101
- Pipin V. V., 2021b, *MNRAS*, **502**, 2565
- Pipin V. V., Kosovichev A. G., 2011, *ApJL*, **727**, L45
- Pipin V. V., Kosovichev A. G., 2019, *ApJ*, **887**, 215
- Pipin V. V., Kosovichev A. G., 2020, *ApJ*, **900**, 26
- Pipin V. V., Sokoloff D. D., Zhang H., Kuzanyan K. M., 2013, *ApJ*, **768**, 46
- Pipin V. V., Pevtsov A. A., Liu Y., Kosovichev A. G., 2019, *ApJ*, **877**, L36
- Prabhu A. P., Singh N. K., Käpylä M. J., Lagg A., 2021, *A&A*, **654**, A3
- Raedler K.-H., 1986, *Astronomische Nachrichten*, **307**, 89
- Rempel M., 2005, *ApJ*, **631**, 1286
- Roberts P., Soward A., 1975, *Astron. Nachr.*, **296**, 49
- Ruediger G., Brandenburg A., 1995, *A&A*, **296**, 557
- Schaeffer N., 2013, *Geochemistry, Geophysics, Geosystems*, **14**, 751
- Schrinner M., 2011, *A&A*, **533**, A108
- Schrinner M., Petitdemange L., Dormy E., 2011, *A&A*, **530**, A140
- Seehafer N., 1990, *Sol. Phys.*, **125**, 219
- Stein R. F., Nordlund Å., 2012, *ApJ*, **753**, L13
- Stenflo J. O., 2013, *A&ARv*, **21**, 66
- Stenflo J. O., Kosovichev A. G., 2012, *ApJ*, **745**, 129
- Sullivan C. B., Kaszynski A., 2019, *Journal of Open Source Software*, **4**, 1450
- Tlatov A., Illarionov E., Sokoloff D., Pipin V., 2013, *MNRAS*, **432**, 2975
- Ugarte-Urra I., Upton L., Warren H. P., Hathaway D. H., 2015, *ApJ*, **815**, 90
- Vidotto A. A., Lehmann L. T., Jardine M., Pevtsov A. A., 2018, *MNRAS*, **480**, 477
- Virtanen I. I., Pevtsov A. A., Mursula K., 2019, *A&A*, **624**, A73
- Virtanen P., et al., 2020, *Nature Methods*, **17**, 261
- Wang Y. M., Nash A. G., Sheeley N. R. J., 1989, *ApJ*, **347**, 529
- Warnecke J., Rheinhardt M., Viviani M., Gent F. A., Tuomisto S., Käpylä M. J., 2021, *ApJ*, **919**, L13
- Yang S., Pipin V. V., Sokoloff D. D., Kuzanyan K. M., Zhang H., 2020, *Journal of Plasma Physics*, **86**, 775860302
- Yeates A. R., 2020, *ApJ*, **898**, L49
- Yeates A. R., Nandy D., Mackay D. H., 2008, *ApJ*, **673**, 544
- Zhang H., Sakurai T., Pevtsov A., Gao Y., Xu H., Sokoloff D. D., Kuzanyan K., 2010, *MNRAS*, **402**, L30

## Appendix

### A. The $\alpha$ -effect, pumping, and eddy diffusivity.

The  $\alpha$ -effect takes into account the kinetic and magnetic helicities,

$$\alpha_{ij} = 3\eta_T C_\alpha \psi_\alpha(\beta) \alpha_{ij}^{(H)} + \alpha_{ij}^{(M)} \frac{\bar{\chi} \tau_c}{4\pi \bar{\rho} \ell^2} \quad (33)$$

where  $C_\alpha$  is a free parameter, the  $\alpha_{ij}^{(H)}$  and  $\alpha_{ij}^{(M)}$  express the kinetic and magnetic helicity coefficients, respectively,  $\bar{\chi}$  is the small-scale magnetic helicity, and  $\ell$  is the typical length scale of the turbulence. The helicity coefficients have been

derived by Pipin (2008). The  $\alpha_{ij}^{(H)}$  reads,

$$\begin{aligned} \alpha_{ij}^{(H)} &= \delta_{ij} \left\{ \left( f_{10}^{(a)} \left( \mathbf{e} \cdot \mathbf{\Lambda}^{(\rho)} \right) + f_{11}^{(a)} \left( \mathbf{e} \cdot \mathbf{\Lambda}^{(u)} \right) \right) \right\} + \quad (34) \\ &+ e_i e_j \left\{ \left( f_5^{(a)} \left( \mathbf{e} \cdot \mathbf{\Lambda}^{(\rho)} \right) + f_4^{(a)} \left( \mathbf{e} \cdot \mathbf{\Lambda}^{(u)} \right) \right) \right\} \\ &+ \left\{ \left( e_i \Lambda_j^{(\rho)} + e_j \Lambda_i^{(\rho)} \right) f_6^{(a)} + \left( e_i \Lambda_j^{(u)} + e_j \Lambda_i^{(u)} \right) f_8^{(a)} \right\}, \end{aligned}$$

where  $\mathbf{e} = \frac{\mathbf{\Omega}}{\Omega}$ ,  $\mathbf{\Lambda}^{(\rho)} = \nabla \log \bar{\rho}$ ,  $\mathbf{\Lambda}^{(u)} = \nabla \log(u' \ell)$  and the  $\alpha_{ij}^{(M)}$  reads:

$$\alpha_{ij}^{(M)} = 2f_2^{(a)} \delta_{ij} - 2f_1^{(a)} e_i e_j, \quad (35)$$

Functions  $f_n^{(a)}(\Omega^*)$  were defined by Pipin (2008),  $\Omega^* = 2\tau_c \Omega_0$ , and  $\Omega_0/2\pi = 432\text{nHz}$ . In the simulations, we use the case  $\varepsilon = 1$  (small-scale magnetic fields in the background turbulence are in equipartition with the kinetic velocity fluctuations).

$$\begin{aligned} f_1^{(a)} &= \frac{1}{4\Omega^{*2}} \left( (\Omega^{*2} + 3) \frac{\arctan \Omega^*}{\Omega^*} - 3 \right), \\ f_2^{(a)} &= \frac{1}{4\Omega^{*2}} \left( (\Omega^{*2} + 1) \frac{\arctan \Omega^*}{\Omega^*} - 1 \right), \\ f_4^{(a)} &= \frac{1}{6\Omega^{*3}} \left( 3(\Omega^{*4} + 6\varepsilon\Omega^{*2} + 10\varepsilon - 5) \frac{\arctan \Omega^*}{\Omega^*} \right. \\ &\quad \left. - ((8\varepsilon + 5)\Omega^{*2} + 30\varepsilon - 15) \right), \\ f_5^{(a)} &= \frac{1}{3\Omega^{*3}} \left( 3(\Omega^{*4} + 3\varepsilon\Omega^{*2} + 5(\varepsilon - 1)) \frac{\arctan \Omega^*}{\Omega^*} \right. \\ &\quad \left. - ((4\varepsilon + 5)\Omega^{*2} + 15(\varepsilon - 1)) \right), \\ f_6^{(a)} &= -\frac{1}{48\Omega^{*3}} \left( 3((3\varepsilon - 11)\Omega^{*2} + 5\varepsilon - 21) \frac{\arctan \Omega^*}{\Omega^*} \right. \\ &\quad \left. - (4(\varepsilon - 3)\Omega^{*2} + 15\varepsilon - 63) \right), \\ f_8^{(a)} &= -\frac{1}{12\Omega^{*3}} \left( 3((3\varepsilon + 1)\Omega^{*2} + 4\varepsilon - 2) \frac{\arctan \Omega^*}{\Omega^*} \right. \\ &\quad \left. - (5(\varepsilon + 1)\Omega^{*2} + 12\varepsilon - 6) \right), \\ f_{10}^{(a)} &= -\frac{1}{3\Omega^{*3}} \left( 3(\Omega^{*2} + 1)(\Omega^{*2} + \varepsilon - 1) \frac{\arctan \Omega^*}{\Omega^*} \right. \\ &\quad \left. - ((2\varepsilon + 1)\Omega^{*2} + 3\varepsilon - 3) \right), \\ f_{11}^{(a)} &= -\frac{1}{6\Omega^{*3}} \left( 3(\Omega^{*2} + 1)(\Omega^{*2} + 2\varepsilon - 1) \frac{\arctan \Omega^*}{\Omega^*} \right. \\ &\quad \left. - ((4\varepsilon + 1)\Omega^{*2} + 6\varepsilon - 3) \right). \end{aligned}$$

The magnetic quenching function of the hydrodynamical part of  $\alpha$ -effect:

$$\psi_\alpha = \frac{5}{128\beta^4} \left( 16\beta^2 - 3 - 3(4\beta^2 - 1) \frac{\arctan(2\beta)}{2\beta} \right). \quad (36)$$

In the model we take into account the mean drift of large-scale field due to the magnetic buoyancy,  $\gamma_{ij}^{(buo)}$  and the gradient of the mean density,  $\gamma_{ij}^{(\Lambda\rho)}$ :

$$\begin{aligned} \gamma_{ij} &= \gamma_{ij}^{(\Lambda\rho)} + \gamma_{ij}^{(buo)}, \\ \gamma_{ij}^{(\Lambda\rho)} &= 3\nu_T f_1^{(a)} \left\{ \left( \mathbf{\Omega} \cdot \mathbf{\Lambda}^{(\rho)} \right) \frac{\Omega_n}{\Omega^2} \varepsilon_{inj} - \frac{\Omega_j}{\Omega^2} \varepsilon_{inm} \Omega_n \Lambda_m^{(\rho)} \right\} \quad (37) \\ \gamma_{ij}^{(buo)} &= \frac{\alpha_{MLT} u_c}{\gamma} \mathcal{H}(\beta) \hat{r}_n \varepsilon_{inj}, \end{aligned}$$

where  $\alpha_{MLT} = 1.9$  is the MESA mixing-length theory parameter,  $\gamma$  is the adiabatic law constant,  $u_c$  is the convective

RMS velocity, and

$$\mathcal{H}(\beta) = \frac{1}{8\beta^2} \left( \frac{3}{\beta} \arctan(\beta) - \frac{(5\beta^2 + 3)}{(1 + \beta^2)^2} \right),$$

(see, [Kitchatinov & Pipin 1993](#); [Ruediger & Brandenburg 1995](#))

We employ the anisotropic diffusion tensor following the formulation of [Pipin \(2008\)](#) :

$$\eta_{ijk} = 3\eta_T \left\{ \left( 2f_1^{(a)} - f_2^{(d)} \right) \varepsilon_{ijk} + 2f_1^{(a)} \frac{\Omega_i \Omega_n}{\Omega^2} \varepsilon_{jnk} \right\} \quad (38)$$

where

$$f_2^{(d)} = \frac{1}{4\Omega^{*2}} \left( ((\varepsilon - 1)\Omega^{*2} + 3\varepsilon + 1) \frac{\arctan(\Omega^*)}{\Omega^*} - (3\varepsilon + 1) \right),$$

and  $\varepsilon = 1$ .

## B. The angular momentum balance and the meridional circulation

Our dynamo model takes into account the effects of the magnetic activity on the angular momentum balance:

$$\begin{aligned} \frac{\partial}{\partial t} \bar{\rho} r^2 \sin^2 \theta \Omega &= -\nabla \cdot \left( r \sin \theta \bar{\rho} \left( \hat{\mathbf{T}}_\phi + r \sin \theta \Omega \bar{\mathbf{U}}^m \right) \right) \quad (39) \\ &+ \nabla \cdot \left( r \sin \theta \frac{\overline{\langle \mathbf{B} \rangle \langle B \rangle}_\phi}{4\pi} \right), \end{aligned}$$

where the overbar means the azimuthal averaging, and  $\langle \mathbf{B} \rangle = \overline{\mathbf{B}} + \tilde{\mathbf{B}}$ . Here,  $\overline{\mathbf{B}}$  and  $\tilde{\mathbf{B}}$  are the axisymmetric and nonaxisymmetric components of the large-scale magnetic field. We find that the magnetic tension contribution can be decomposed into sum:  $\overline{\mathbf{B}B}_\phi + \overline{\tilde{\mathbf{B}}\tilde{B}}_\phi$ , where the second part represents the longitudinal average of the magnetic tensions from the non-axisymmetric magnetic fields. The meridional circulation is governed by equation for the azimuthal component of large-scale vorticity,  $\bar{\omega} = (\nabla \times \bar{\mathbf{U}}^m)_\phi$ :

$$\begin{aligned} \frac{\partial \omega}{\partial t} &= r \sin \theta \nabla \cdot \left( \frac{\hat{\phi} \times \nabla \cdot \bar{\rho} \hat{\mathbf{T}}}{r \bar{\rho} \sin \theta} - \frac{\bar{\mathbf{U}}^m \bar{\omega}}{r \sin \theta} \right) \quad (40) \\ &+ r \sin \theta \frac{\partial \Omega^2}{\partial z} - \frac{g}{c_p r} \frac{\partial \bar{s}}{\partial \theta} \\ &+ \frac{1}{4\pi \bar{\rho}} \overline{(\langle \mathbf{B} \rangle \cdot \nabla) (\nabla \times \langle \mathbf{B} \rangle)_\phi} \\ &- \frac{1}{4\pi \bar{\rho}} \overline{((\nabla \times \langle \mathbf{B} \rangle) \cdot \nabla) \langle \mathbf{B} \rangle_\phi}, \end{aligned}$$

where  $\hat{\mathbf{T}}$  is the turbulent stress tensor. Also,  $\bar{\rho}$  is the mean density,  $\bar{s}$  is the mean entropy;  $\partial/\partial z = \cos \theta \partial/\partial r - \sin \theta/r \cdot \partial/\partial \theta$  is the gradient along the axis of rotation. The second line accounts for the source terms of the meridional circulation, which are due to the centrifugal and baroclinic forces. We neglect the effects of the rotational oblateness of the density and pressure profiles. More details about this part of the model as well as the model of the mean-field heat transport can be found in [Pipin & Kosovichev \(2019\)](#). We plan to discuss the effects of the magnetic tensions, which results from the BMRs evolution, in a separate paper.